Article

Electrochemical Growth and Structural Study of the Al$_x$Ga$_{1-x}$As Nanowhisker Layer on the GaAs Surface

Yana Suchikova [1,*] , Sergii Kovachov [1] , Ihor Bohdanov [1], Anar A. Abdikadirova [2], Inesh Kenzhina [3,4] and Anatoli I. Popov [2,5,*]

1   The Department of Physics and Methods of Teaching Physics, Berdyansk State Pedagogical University, 71100 Berdyansk, Ukraine; essfero@gmail.com (S.K.); bogdanovbdpu@gmail.com (I.B.)
2   Faculty of Economics, Department of State Audit, L.N. Gumilyov Eurasian National University, 2 Saybayev Street, Astana 010000, Kazakhstan; a.abdikadirova@mdai.gov.kz
3   Department of General Physics, Satbayev University, Almaty 050032, Kazakhstan; kenzhina@physics.kz
4   Advanced Electronics Development Laboratory, Kazakh-British Technical University, Almaty 050000, Kazakhstan
5   Institute of Solid State Physics, University of Latvia, LV-1063 Riga, Latvia
*   Correspondence: yanasuchikova@gmail.com (Y.S.); popov@latnet.lv (A.I.P.)

Abstract: This work presents a novel, cost-effective method for synthesizing Al$_x$Ga$_{1-x}$As nanowhiskers on a GaAs surface by electrochemical deposition. The process begins with structuring the GaAs surface by electrochemical etching, forming a branched nanowhisker system. Despite the close resemblance of the crystal lattices of AlAs, GaAs, and Al$_x$Ga$_{1-x}$As, our study highlights the formation of nanowhiskers instead of layer-by-layer film growth. X-ray diffraction analysis and photoluminescence spectrum evaluations confirm the synthesized structure's crystallinity, uniformity, and bandgap characteristics. The unique morphology of the nanowhiskers offers promising implications for solar cell applications because of the increased light absorption potential and reduced surface recombination energy losses. We conclude by emphasizing the need for further studies on the growth mechanisms of Al$_x$Ga$_{1-x}$As nanowhiskers, adjustments of the "x" parameter during electrochemical deposition, and detailed light absorption properties of the formed compounds. This research contributes to the field of wideband materials, particularly for solar energy applications, highlighting the potential of electrochemical deposition as a flexible and economical fabrication method.

Keywords: nanowhiskers; electrochemical deposition; electrochemical etching; crystal lattice; layer-by-layer growth; X-ray diffraction analysis; photoluminescence spectrum; crystallinity

1. Introduction

The advancement of modern electronics and solar energy technologies encourages researchers worldwide to explore new materials with enhanced properties [1,2]. Today, methods of semiconductor technology are actively developing, enabling the production of a broad class of materials with tunable properties depending on the ratio of components [3–15]. Thus, ternary compounds based on Cd$_x$Te$_y$O$_z$ alter their properties depending on the concentration of Cd and Te in the alloy [16,17]. Similar conclusions were obtained for CuGa$_x$In$_{1-x}$Se$_2$ and other compounds [18,19].

Another effective way to tune the properties of materials is by surface nanostructuring [20–22]. It has been repeatedly shown that simple electrochemical treatment methods can significantly impact the macro- and microarchitecture of semiconductor surfaces [23]. For example, a wide range of electrolytes is known today for group A3B5 materials and silicon [24]. In general, silicon remains in a leading position in the microelectronics industry [25]. However, for many applications in energy conversion, preference is given to group A3B5 materials, such as InP, GaP, and GaAs [26]. In turn, GaAs is a direct competitor to silicon technology [27]. This material has high charge carrier mobility, low dielectric

permeability, and high absorbance [28]. On the other hand, gallium arsenide has a bandgap in the region of 1.42 eV, which somewhat limits its application range. Many technologies have been developed to expand these prospects to create ternary compounds based on GaAs [29,30]. For example, it has been shown that alloying it with indium atoms makes it possible to create the ternary compound $In_xGa_{1-x}As$ [31]. The more indium in the compound, the more we observe a shift of the electromagnetic spectrum in the infrared region of the spectrum to a minimum value of 0.354 eV [32]. This expands the application of $In_xGa_{1-x}As$, particularly as materials for infrared optics [33].

On the other hand, there is also a current demand for wide-bandgap semiconductors (WBG) [34]. Such semiconductors allow power electronics components to be smaller, faster, more reliable, and more efficient [35]. They also typically have higher electron mobility and saturation speed, ensuring higher switching frequencies [36]. Finally, components made from WBG semiconductors also operate at higher voltages and temperatures than conventional semiconductor materials [37].

To expand the bandgap of GaAs, technologies for doping it with aluminum have been proposed [38]. These technologies include molecular beam epitaxy, liquid phase epitaxy, and vacuum deposition [39,40]. Typically, these methods require high-tech equipment, long processing times, high temperatures, a vacuum, and significant resources. All of these slow down the progress in applying such materials on an industrial scale. In contrast to these methods, researchers are increasingly focusing on simple and inexpensive techniques: electrochemical and chemical etching, electrochemical deposition, and combinations [41,42]. The advantages of these methods are their cost-effectiveness, simplicity, and short processing times [43,44]. The disadvantages usually include weak process controllability and a high probability of surface contamination by the reaction products [45]. Therefore, further development of electrochemical technologies remains a relevant task.

The electrochemical treatment of group III–V semiconductors in acidic electrolyte solutions leads to the formation of porous layers, surface texture, and nanostructuring with the formation of crystallites, nanoneedles, nanowires, etc. [46]. At the same time, alternative electrochemical reactions, specifically the deposition of dissolution products on the semiconductor surface, can often occur at the electrolyte–semiconductor interface [47]. This can result in the formation of dense films or the growth of nanostructured crystallites [48]. These effects have piqued the interest of many researchers, prompting them to explore various electrolyte compositions for controlled electrochemical deposition processes [49].

In this work, we report synthesizing the ternary compound $Al_xGa_{1-x}As$ on a GaAs substrate by electrochemical deposition. A unique feature of this process is the preliminary preparation of the GaAs surface, specifically, electrochemical texturing. This, in turn, allowed the formation of not a continuous $Al_xGa_{1-x}As$ film but a system of branched nanowhiskers. In this study, we attempt to explain the nature of such behavior and investigate some structural and optical characteristics of $Al_xGa_{1-x}As$.

2. Materials and Methods

2.1. Experimental Method

For the growth substrate of the $Al_xGa_{1-x}As$ compound, a monocrystalline gallium arsenide of n-type conductivity, doped with Sb, was chosen. The plates had a surface orientation of (111). Before the experiment, the samples were carefully prepared. The samples were treated in an aqueous hydrochloric acid solution. This step is necessary for surface polishing and to remove passivating surface layers that may form on the surface of GaAs when stored in the air. The samples were immersed in an HCl solution (HCl: H_2O = 1:5 by mass) and kept at room temperature for 30 min. After this, the samples were cleaned of possible reaction products in vinegar and alcohol.

After being cleaned, the samples were immediately used in the experiment to prevent oxidation of the prepared surface.

A porous layer was formed on the mono-GaAs surface by electrochemical etching in a hydrochloric acid aqueous solution with a component ratio of HCl:H_2O = 1:4 (by mass).

Electrochemical etching was carried out in a standard three-electrode cell for 7 min with a constant potential U = 5 V applied. During the electrochemical etching, the electrolyte solution turned pink, indicating the arsenic substrate's predominant dissolution and the introduction of its atoms into the electrolyte. At this stage, no observations of the change in the sample morphology were made to prevent oxidation.

Immediately after electrochemical etching, the process moved to form $Al_xGa_{1-x}As$ nanowhiskers.

Nanowhiskers were grown by the method of electrochemical deposition. For this, an aqueous solution of $AlCl_3$ was used. To prepare this electrolyte, anhydrous crystals of $AlCl_3$ were dissolved in water at a 2:3 mass ratio at a temperature of 25 °C. For better dissolution, a magnetic stirrer was used, which stirred the electrolyte for 10 min. $AlCl_3$ dissolves well in water to form aluminum hydroxide:

$$AlCl_3 + 3H_2O \rightarrow Al(OH)_3 + 3HCl, \tag{1}$$

After this, the GaAs samples were immersed in the prepared electrolyte solution. The electrochemical growth cell used for deposition had a three-electrode configuration consisting of a platinum electrode (Pt), a silver/silver chloride auxiliary electrode Ag/AgCl (RE), and a GaAs semiconductor plate. The treated Teflon crucible was modified compared with previous designs, namely, it was equipped with a stirrer to remove bubbles and the uniform arrival of the electrolyte to the substrate surface. The reference electrode was connected to the growth cell through a salt bridge to prevent contamination of the deposited films. The electrochemical deposition was performed in cycles. One cycle included holding the sample in the electrolyte for 2 min at U = 3 V and 1 min at U = 6 V. A total of three such cycles were performed. The potential is held constant at these values during their respective time intervals. Figure 1 presents a schematic representation of the current density and voltage changes during the experiment over three cycles. It can be observed that over time, the rate of growth of the current density decreases. This indicates a slowing down of the active phase of nanowhiskers' growth. The mechanism behind this phenomenon will be discussed further below.
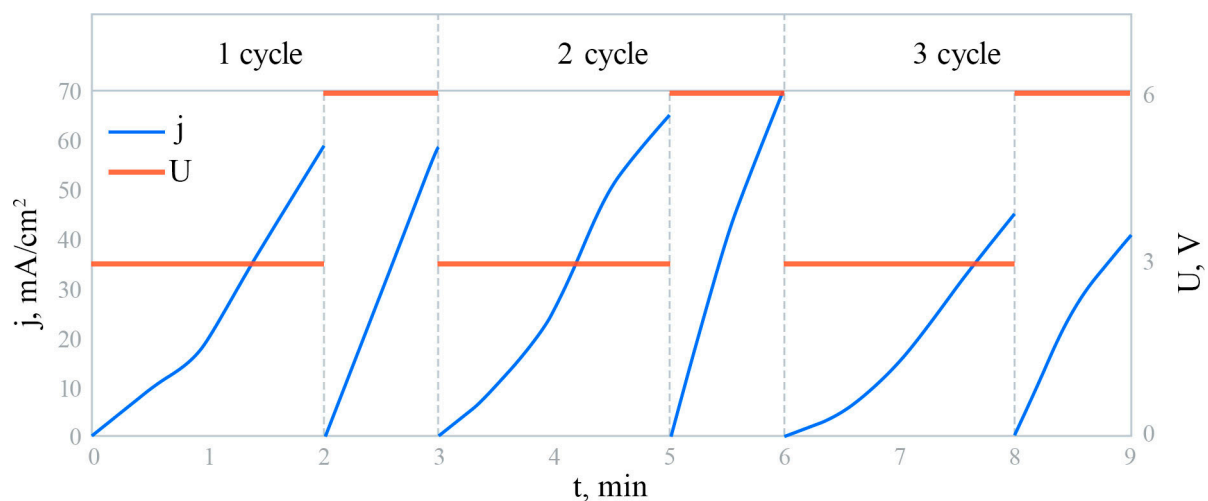
Figure 1. Schematic representation of the changes in current density and voltage during the experiment over three cycles.

It should be noted that the deposition of materials by cyclic voltammetry is one of the standard methods of synthesizing nanostructures, particularly nanowhiskers [50]. During this process, a critical stage is the formation of nucleation centers, which serve as the basis for the further growth of nanowhiskers, preventing the formation of continuous films. The method we applied is similar to the standard Pulse Electrodeposition (PED) method, which typically involves changing the applied potential in a pulsating manner

to control the deposition process. In the standard PED process, the applied potential or current density often alternates between two or more levels, with a deposition phase and a relaxation or dissolution phase. The presented method is a simplified or specific form of pulse deposition.

2.2. Research Methods

The morphology of the samples was investigated using the SEO-SEM Inspect S50-B scanning electron microscope. The microscope was equipped with an AZtecOne energy-dispersive analysis detector, allowing for component composition analysis at points and surface mapping. Furthermore, the phase and surface states were investigated using Raman spectroscopy on a RENISHAW inVia Reflex microspectrometer (conditions: room temperature; laser wavelength λ = 532 nm; grid 2400 nm; range 100–1000 cm^{-1}; measurement time 10 s; 5 accumulations; laser intensity 5%). The Dron-3M equipment was used for the structural analysis (range of angles 2 = 10–80°, step 0.01). The photoluminescence was investigated using the KSVU-23 spectral setup at room temperature. A laser with a wavelength of 450 nm was used as the excitation source.

3. Results

3.1. SEM Analysis

As mentioned in the Section 2, we refrained from performing morphological observations immediately after the electrochemical etching step to prevent oxidation. However, for a more comprehensive understanding and to demonstrate the formation of the porous layer on the GaAs surface, we evaluated the morphology of samples prepared under similar conditions (Figure 2).
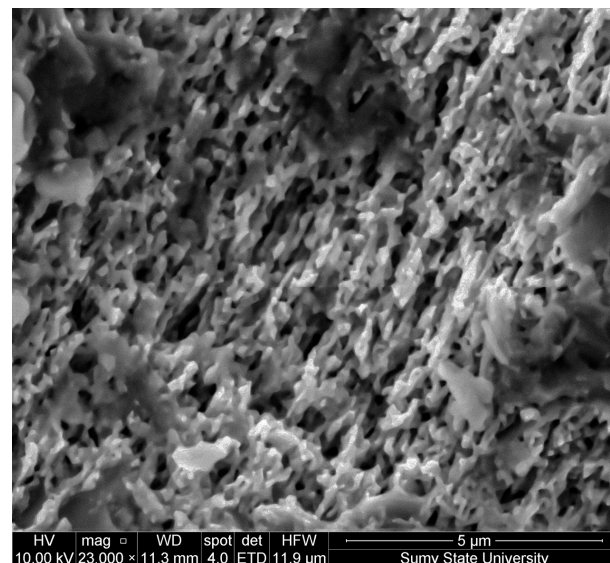

Figure 2. SEM of porous GaAs synthesized by electrochemical etching in HCl:H_2O (1:4 by mass) for 7 min at U = 5 V.

It can be observed that the GaAs surface is densely covered with a porous layer. The pores manifest as systematically ordered openings, and, notably, these pores exhibit heightened anisotropy and are distinctly oriented along the crystallographic direction. The porous gaps impart a pronounced surface texturing, enhancing its effective area. The intricate morphology of the porous GaAs can serve as an excellent buffer layer for the growth of nanowhiskers. Such a structure ensures optimal conditions for the development and adhesion of nanowires, owing to its high surface activity and unique morphology.

As a result of the electrochemical deposition, a system of nanowhiskers was formed on the GaAs surface (Figure 3a). Nanowhiskers have cross-sectional diameters ranging from 70 to 100 nm, and the length varies widely from 0.5 to 2 μm (Figure 3b). The system

of nanowhiskers is disordered and has no defined directions. The nanowhiskers intersect at 45° and 90° angles (Figure 3c). The star-shaped structure indicates that whisker growth occurred from nucleation centers on the substrate surface (Figure 3d). It can also be seen that fluffy clouds are present on the surface, which could be an amorphous phase of native oxide (Figure 3e). GaAs was previously shown to be prone to surface oxidation during electrochemical treatment, forming gallium, arsenic oxides, or complex ternary compounds [51,52].
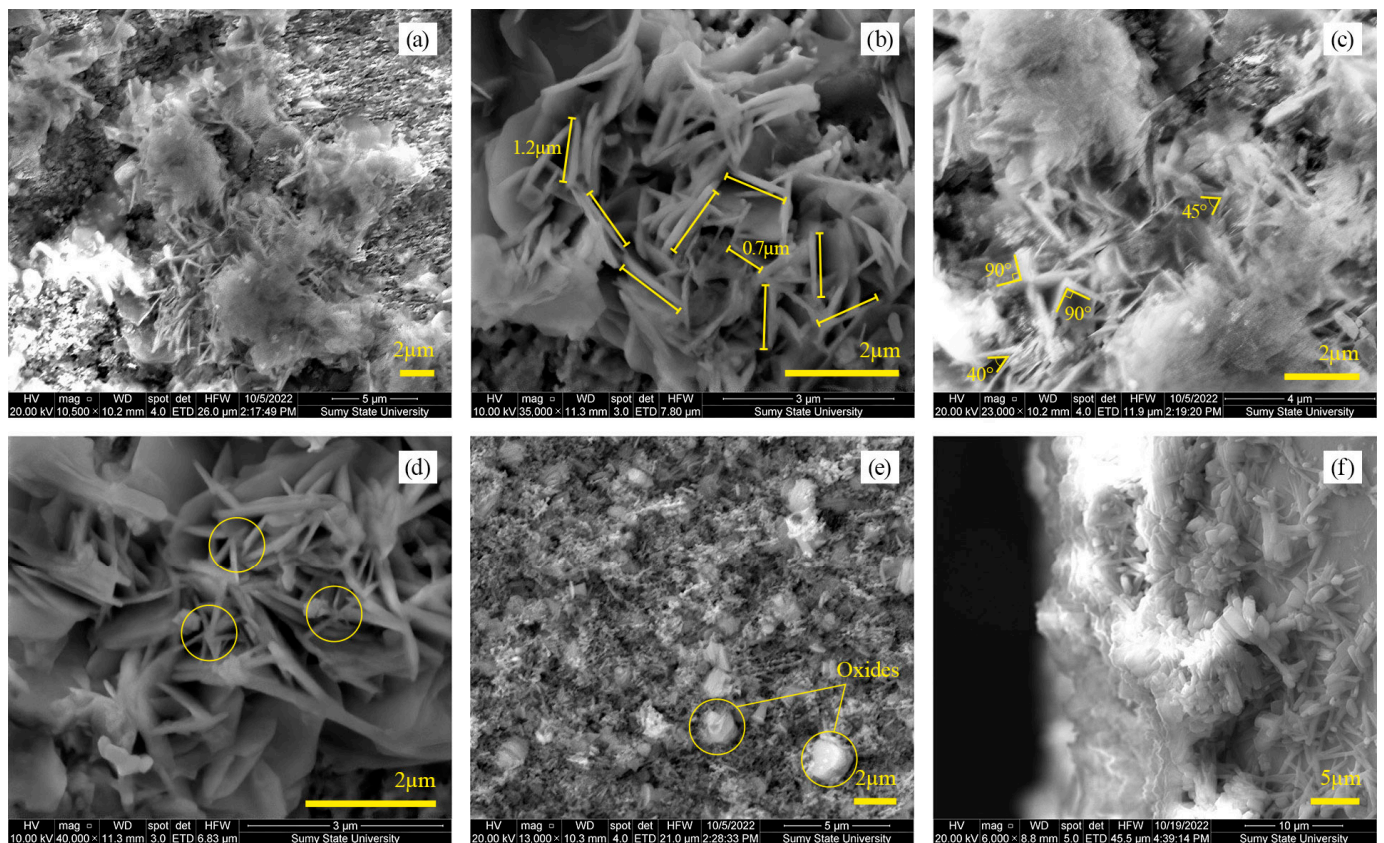
Figure 3. SEM characterization of $Al_xGa_{1-x}As$ nanowhiskers: (**a**) Top view showing nanowhiskers on the GaAs surface; (**b**) Dimensions of nanowhiskers with diameters 70–100 nm and lengths 0.5–2 μm; (**c**) Intersection angles of 45° and 90°; (**d**) Star-shaped nucleation patterns; (**e**) Possible amorphous native oxide formations; (**f**) Cross-sectional view of nanowhisker.

The nanowhiskers are packed into islands that evenly cover the GaAs surface in a dense layer. The cross-sectional diameters of the islands range from 2 to 7 μm. The thickness of the coating varies in different areas from 5 to 15 μm (Figure 3f).

3.2. EDX Analysis

The elemental composition of the compound was studied using energy-dispersive X-ray spectroscopy at several points on the sample surface to ensure the data representativeness of the obtained compound (Table 1). Additionally, elemental distribution mapping was performed on the compound surface to visualize the heterogeneity and homogeneity of the elemental composition (Figure 4). From an analysis of Table 1, it can be seen that the percentage ratio of As, Ga, and Al in the compound changes slightly between different points, indicating the relative uniformity of the component ratio in the compound. Oxygen (O) is also present in the compound, but its concentration is negligible, indicating partial surface oxidation. The surface analysis of the sample obtained by mapping also confirms the homogeneity of the element distribution on the surface. The oxidation of the surface layers may result from the partial interaction of the elements with the solvent ions. Oxidation

may occur through free radicals that form during the electrochemical reaction and electron transfer between the substrate and the solution. Furthermore, surface oxidation may occur even after the completion of the electrochemical treatment process of the samples because of the presence of broken bonds at the tops of the nanowhiskers.

Table 1. Elemental composition of the $Al_xGa_{1-x}As$ surface, obtained using the EDX method.

Elements	At, %			
	1	2	3	4
O	7.35	6.23	7.01	6.91
As	41.54	42.12	40.69	42.05
Ga	26.74	26.95	26.51	27.14
Al	24.37	24.7	25.79	23.90
Total	100	100	100	100
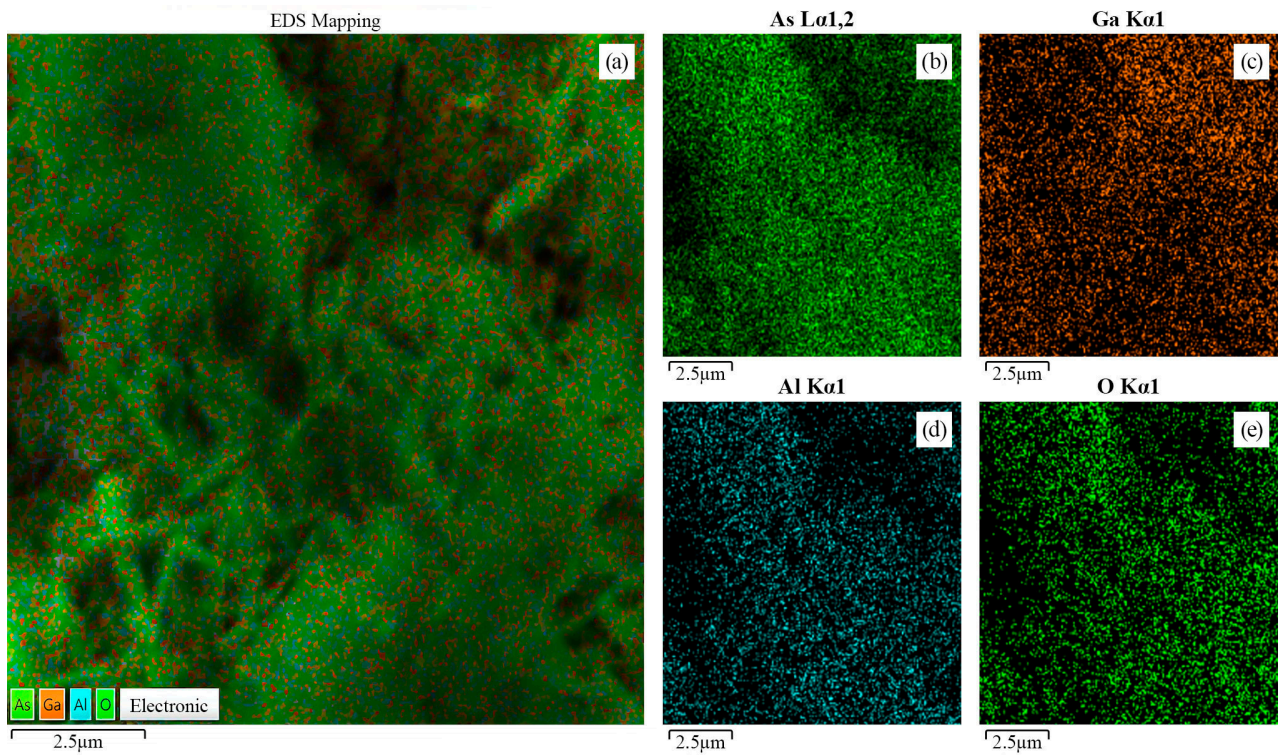
Figure 4. Energy-dispersive (EDX) mapping analysis of the surface $Al_xGa_{1-x}As$: (**a**) Composite image showing all elements; (**b**) Distribution of As; (**c**) Distribution of Ga; (**d**) Distribution of Al; (**e**) Distribution of O.

Table 2 shows the relative ratios of the elements Ga, Al, and As at four points in the sample. The relative ratios were calculated based on the atomic ratios of the components presented in Table 1.

Table 2. The ratio of components on the surface $Al_xGa_{1-x}As$.

Elements	Relative Units, %			
	1	2	3	4
Ga/As	0.64	0.64	0.65	0.65
Al/As	0.59	0.59	0.63	0.57
Al/Ga	0.911	0.916	0.973	0.881
(Al + Ga)/As	1.23	1.23	1.28	1.22

The Ga/As and Al/As ratios are not significantly different, but Ga predominates over Al. On the other hand, the Ga/As ratio is 0.64 and 0.65 for different sample points. One hypothesis for the observed decrease in the Ga/As ratio is that Al is replacing Ga atoms on the GaAs surface. This is due to the interaction of the GaAs surface with the electrolyte solution. At the same time, the (Al + Ga)/As ratio across the entire surface is >1, indicating that the deposition of aluminum also occurred at the expense of the partial loss of As. We also observed an electrochemical dissolution reaction of the GaAs surface during the electrochemical deposition. This was evidenced by the change in the solution's color to a grayish-pink hue, an increase in its turbidity, and the appearance of a dark precipitate on the platinum electrode. Furthermore, the deposition was carried out on an already prepared etched GaAs surface, which could potentially disrupt the stoichiometric GaAs ratio. The authors would like to emphasize that the elemental composition measurements presented in this study are intended to serve as a semiquantitative means of demonstrating the electrochemical deposition of Al onto the surface of GaAs to form $Al_xGa_{1-x}As$ whiskers. However, this analysis allows us to present some considerations about the electrochemical processes at the $AlCl_3$—GaAs system interface, which will be explained later in the Section 4.

3.3. XRD Analysis

Figure 5 shows the diffractometric pattern of the formed structure. It can be seen that the main peak corresponds to the plane (111) of $Al_xGa_{1-x}As$. Three other intense peaks at angles 2θ = 45.55, 53.75, and 65.55° correspond to the (220), (311), and (400) planes, respectively. Furthermore, there are several less intense peaks at 2θ = 61.95, 66.7, 72.10, and 74.65°.
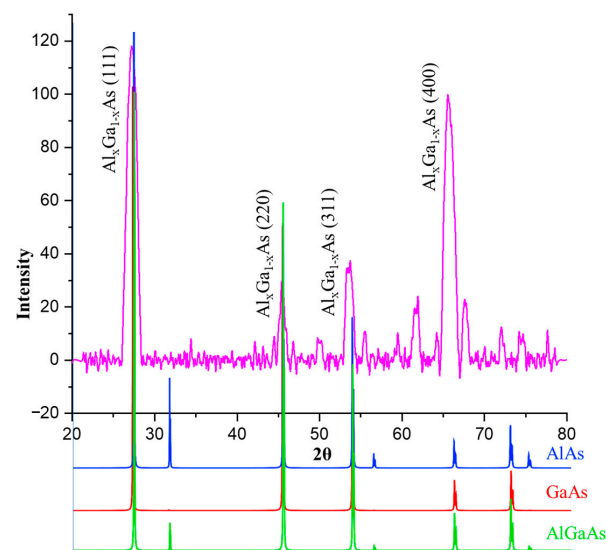
Figure 5. XRD spectrum of $Al_xGa_{1-x}As$ with overlaid reference spectra AlAs, GaAs, and AlGaAs from the Crystallography Open Database (COD) visualized using the VESTA program.

The main peak corresponds to the cubic $Al_{0.71}Ga_{0.29}As$ structure (Reference code: 00-051-1089). Such a peak is also characteristic of AlAs and GaAs. The peaks at 2θ = 53.75° and 65.55° also correspond to the ternary alloy $Al_xGa_{1-x}As$. However, compared to the reference spectra, a leftward shift is observed. The peaks at 2θ = 66.7° and 72.10° are characteristic of AlAs, GaAs, and AlGaAs with a slight shift to the left side of the spectrum, whereas the peaks at 2θ = 74.65° are identified as peaks from cubic AlAs and AlGaAs.

The peak at 2θ = 61.95° could be attributed to oxides, notably A_2O_3.

The XRD data, shown in Figure 3, were used in conjunction with the Scherrer equation to determine the average crystallite size. The Scherrer equation is given as follows [53]:

$$D = \frac{K\lambda}{\beta \cos \theta} \qquad (2)$$

where D is the average crystallite size; K represents the shape of the crystallite; λ is the wavelength of the CuKα_1 X-ray radiation (1.540598 Å); B is the full width at half maximum (FWHM) in radians; and θ is the diffraction angle (within Bragg's limits).

In this case, the shape factor K was set to 0.89 due to the cubic crystalline symmetry [54]. For the obtained film, the diffraction peak (111), which is the most intense, was used to determine the average crystallite size of 60.49 nm.

$Al_xGa_{1-x}As$ is a ternary compound, with AlAs as the boundary case when x = 1 and GaAs when x = 0. The inclusion of Al in the GaAs structure significantly alters its properties. In the $Al_xGa_{1-x}As$ ternary compound, Al does not simply act as a dopant. Instead, it assumes a more critical role. As the concentration of Al (represented by 'x') increases, it affects not only the lattice structure but also the material's bandgap and other electronic properties. Specifically, introducing Al changes the material's bandgap, rendering it tunable based on the Al concentration [38–40]. This bandgap tunability is one of the compelling reasons why $Al_xGa_{1-x}As$ compounds have piqued considerable interest in optoelectronic applications.

It can be observed from Table 3 and Figure 4 that the crystal lattices of AlAs, GaAs, and $Al_xGa_{1-x}As$ are strikingly similar. Given the near-congruence of the crystal lattice parameters of AlAs and GaAs, both of which crystallize in the same space group, it poses a challenge to identify one of the substances in isolation. However, it can be definitively stated that the structure exhibits good crystallinity. The schematic representation in Figure 6 aims to highlight this substitutional behavior of the Al atoms in the GaAs structure.
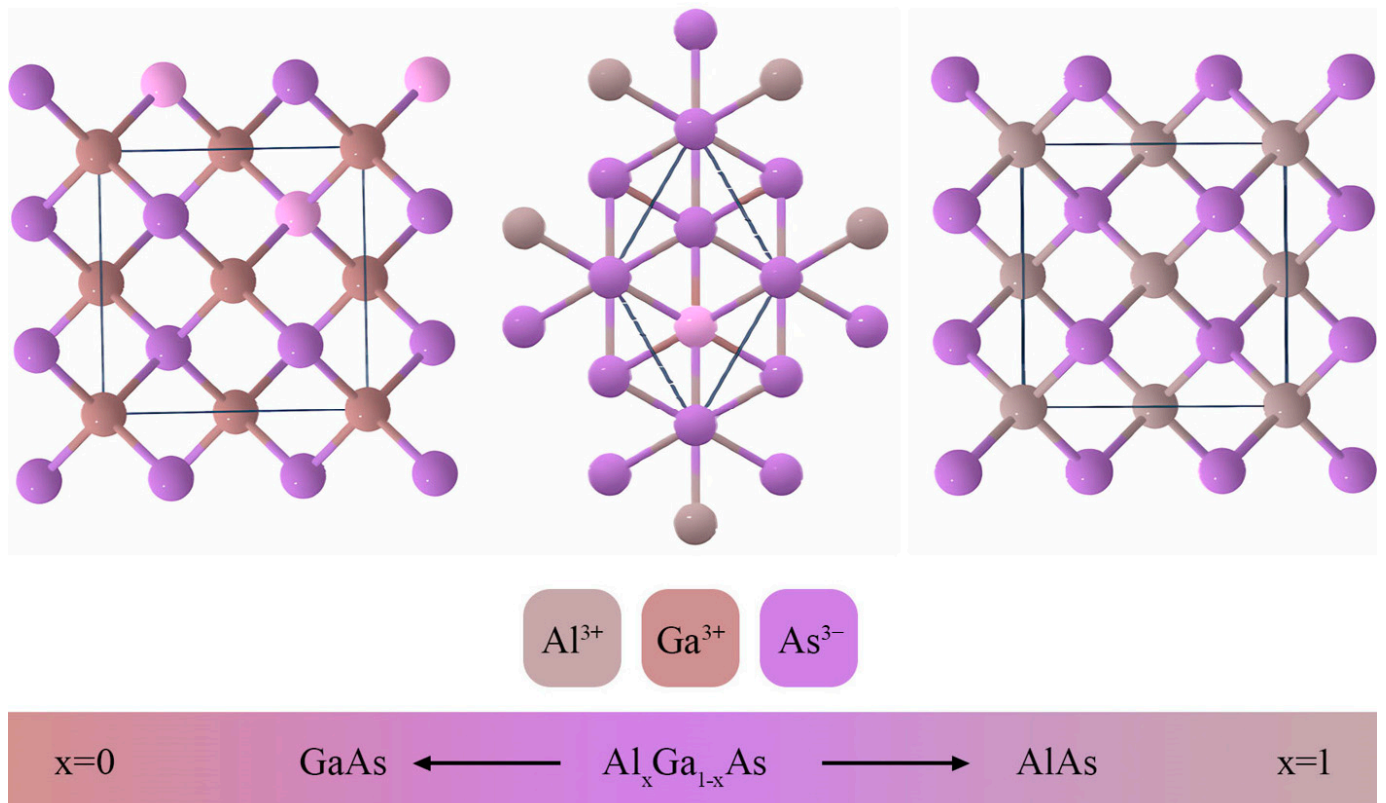

Figure 6. Schematic representation of crystal lattices for AlAs, $Al_{0.71}Ga_{0.29}As$, GaAs.

Table 3. Crystal lattice parameters for AlAs, $Al_{0.71}Ga_{0.29}As$, GaAs.

Parameters	AlAs	$Al_{0.71}Ga_{0.29}As$	GaAs
Crystal system	Cubic	Cubic	Cubic
Space group	F-43m	F-43m	F-43m
Space group number	216	216	216
a = b = c (A)	5.6620	5.6604	5.5080
$\alpha = \beta = \gamma$ (o)	90.00	90.00	90.00
Calculated density (g/cm^3)	3.73	4.19	5.75
Volume of cell (106 pm^3)	181.51	181.36	167.10

3.4. Raman Analysis

For the $Al_xGa_{1-x}As$ material, typical Raman scattering peaks are generally between 260–290 cm^{-1} and 360–390 cm^{-1} [55]. The relative positions of the peaks depend on the structural organization of the alloy and the content of Al. That is, the Raman spectra can differ due to the difference in the concentration of Al and Ga in the alloy. The combination scattering peaks observed in the $Al_xGa_{1-x}As$ alloy are due to the broad exciton luminescence induced by intrinsic defects and the As cluster (Figure 7, Table 4). Fourth-order resonance Raman peaks are observed in the compound's initial resonance state. These resonance peaks were assigned according to their fundamental modes, among which combined bands of GaAs- or AlAs-like modes exist. The presence of four strongly pronounced peaks at 110, 267, 369, and 559 cm^{-1} is observed.
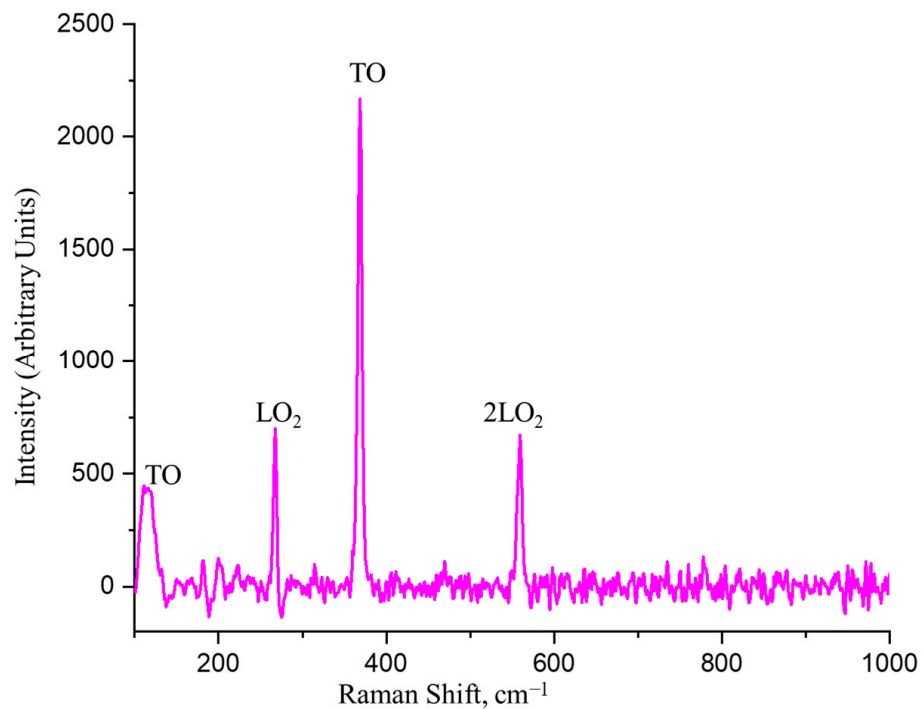
Figure 7. Raman spectrum $Al_xGa_{1-x}As$.

Table 4. Identification of Raman spectrum peaks $Al_xGa_{1-x}As$.

Parameters	Identification		
	Raman Shift	Phonon Mode	Assignment
1	110	TO	Ga-As, Al-As
2	267	LO_2	Ga-As
3	369	TO	Al-As
4	559	$2LO_2$	Ga-As

The peak at 267 cm^{-1} can be associated with GaAs' optical longitudinal (LO) mode, specifically with LO$_{2(GaAs)}$. This peak reflects longitudinal optical oscillations corresponding to Ga-As bonds. LO2$_{(GaAs)}$ corresponds to a higher energy level of longitudinal optical phonons of GaAs. It manifests itself as a result of the interaction between Ga and As atoms in the crystalline structure of Al$_x$Ga$_{1-x}$As and indicates the vibrational mode that occurs between them.

The peak at 369 cm^{-1} in the Al$_x$Ga$_{1-x}$As material can be associated with the transverse optical (TO) mode of AlAs. It reflects transverse optical oscillations of atoms in the Al$_x$Ga$_{1-x}$As structure, corresponding to Al-As bonds. This peak may result from the interaction between Al and As atoms in the crystalline structure and indicates a vibrational mode between them. The intensity of this peak is the highest. Generally, the peaks at 267 and 369 cm^{-1} are typical for the Al$_x$Ga$_{1-x}$As family of materials [56,57].

The peak at 110 cm^{-1} could be associated with a phonon mode or vibrational process in the material occurring at low frequencies. It may result from vibrational modes associated with local inhomogeneities or defects in the crystalline structure. The corresponding peak may reflect atom vibrations around defects or traps, such as vacancies, interstitial atoms, or dislocations.

Lastly, the peak at 559 cm^{-1} in the Al$_x$Ga$_{1-x}$As material could be associated with the second harmonic of the optical longitudinal phonon mode of Ga-As in the Al$_x$Ga$_{1-x}$As alloy, known as 2LO$_{2(GaAs)}$ [58]. This peak results from the double energy transfer of optical longitudinal phonons (LO) between Ga and As atoms in the crystalline structure of the alloy. The second harmonic (2LO) reflects the interaction of two phonons with the same frequencies, creating a new phonon with a frequency equal to the sum of the frequencies of the two initial phonons. In this case, the peak at 559 cm^{-1} reflects the interaction of two optical longitudinal phonons occurring in the Al$_x$Ga$_{1-x}$As structure.

Overall, the spectrum demonstrates good quality, the absence of additional noise, and broadened peaks. This indicates good crystallinity of the obtained structure and the lack of different phases.

3.5. PL Analysis

The photoluminescence spectrum taken at room temperature demonstrates the presence of two peaks, at 600 nm and 850 nm (Figure 8).
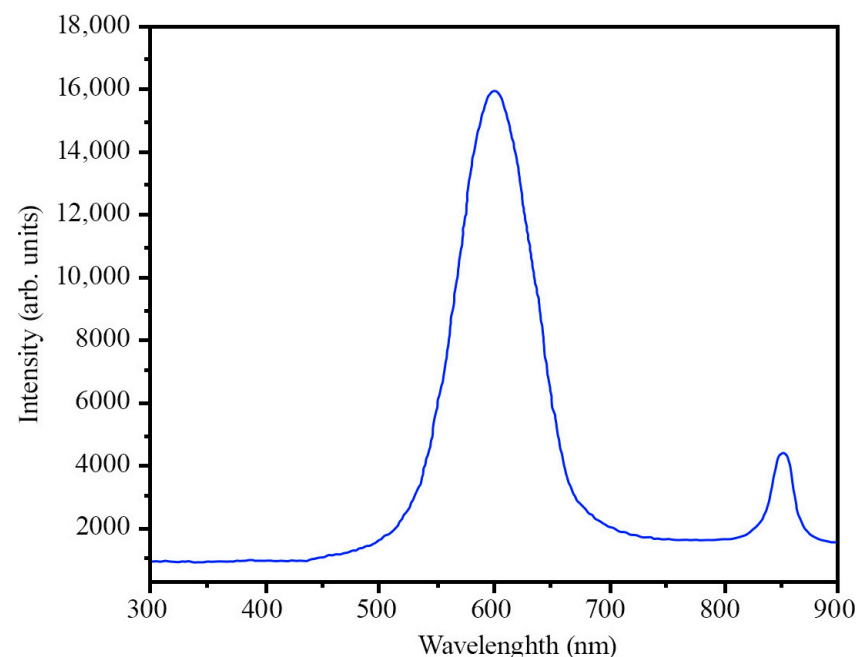
Figure 8. Spectrum of photoluminescence Al$_x$Ga$_{1-x}$As.

The bandgap of $Al_xGa_{1-x}As$ depends on the aluminum content x. The bandgap Eg of the $Al_xGa_{1-x}As$ material family is in the range from 1.42 eV (GaAs) to 2.16 eV (AlAs) [59]. At room temperature (300 K), the dependence of the direct gap on the aluminum content x can be calculated by the equation [60]:

$$Eg(x) = 1.422 \text{ eV} + 1.2475x \text{ eV}, \tag{3}$$

where x is the aluminum fraction in the $Al_xGa_{1-x}As$ alloy.

The theoretical Eg = 2.016 eV matches the experimental data (λ = 600 nm, Eg = 2.067 eV). This confirms the formation of a compound with the formula $Al_{0.71}Ga_{0.29}As$ and is in good agreement with the results of the XRD analysis.

It is worth noting that the second peak at 850 nm (approximately 1.46 eV) can be attributed to the direct bandgap of GaAs or related defects or localized states in the material. Various factors, including structural defects, impurities, carrier recombination mechanisms, and thermal effects, can influence photoluminescence spectra. Therefore, careful consideration of all possible sources of the observed peaks is necessary to comprehensively understand the material's properties.

Also, remember that energy bandgaps estimated from photoluminescence measurements may differ slightly from those calculated using other methods (like absorption or reflection spectroscopy) due to various effects, like Stokes shift or localized states in the material. However, good agreement between different methods confirms the material's high quality and the measurements' reliability.

4. Discussion

To explain the formation of porous GaAs islands consisting of nanowhiskers on the surface, a qualitative model based on the interaction of binary semiconductors with the electrolyte solution has been proposed. The electrochemical dissolution of semiconductors occurs in the electrolyte under the action of the applied potential. At the first stage of processing (electrochemical etching of GaAs), the formation of adatoms that contain semiconductor ions bound with electrolyte ions occurs. These adatoms form transitional layers in the semiconductor–electrolyte system (Gouy-Helmholtz layer) [61]. Under the action of the applied potential, adatoms are torn from the semiconductor surface. Usually, the arsenic substrate is etched at a higher rate than gallium [62]. This leads to the enrichment of the GaAs surface with Ga ions that have broken bonds. After this etching stage, the GaAs surface first acquires a developed morphology and contains many surface states.

The broken bonds and microprotrusions on the surface, formed as a result of the electrochemical etching of GaAs, become the nucleation centers (nucleation sites) for the formation of $Al_xGa_{x-1}As$ nanowhiskers at the second stage (electrodeposition). The adsorption of aluminum atoms occurs. These atoms begin to form nanocrystalline structures, which serve as the basis for the further growth of nanowhiskers. At the same time, a reverse process partially occurs—tearing out Al-Ga adatoms from the sample surface, which then leads to a slight depletion of the surface with Ga atoms.

As the number of adsorbed atoms on the substrate surface increases, nanocrystals merge and become the basis for the growth of nanowhiskers.

In the final stage, nanowhiskers grow until they reach a certain saturation or steady state. In this process, nanowhiskers can be packed into islands through interaction with neighboring nanowhiskers or constraints imposed on the growth in respective directions. Interactions between neighboring nanowhiskers lead to the formation of these islands, limiting the availability of Ga on the GaAs surface for substitution. This results in a slowdown in the growth rate of the nanowhiskers. Moreover, at this stage, the electrolyte can be depleted. Over time, the concentration of active agents in the solution decreases, limiting their availability for nanostructure growth.

If the electrochemical deposition process continues further, several undesirable effects might arise. This includes uneven deposition, the emergence of defects in the structure, and the potential agglomeration of nanowhiskers. Such agglomeration can alter the optical

and electronic properties of the nanowhiskers, making them less suitable for potential applications. Therefore, monitoring the process and timely termination are crucial for optimizing the properties of nanowhiskers.

The packing of nanowhiskers can depend on various factors, such as the concentration of atoms on the surface, the deposition rate, the temperature, and the growth time.

The simplified overall reaction for the electrodeposition process can be represented as:

$$GaAs + Al^{3+} + 3e^- \rightarrow Al_xGa_{1-x}As, \tag{4}$$
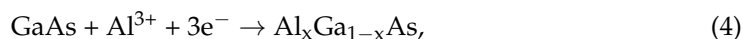
However, it is important to note that this is a very simplified representation, and the actual process could involve multiple intermediate steps, including the possible reduction of Al ions, the incorporation of Al into the GaAs matrix, and the simultaneous dissolution of small amounts of Ga and As. The detailed mechanism would require a comprehensive investigation, including in-situ spectroscopy during electrodeposition.

This growth mechanism of islands and nanowhiskers can explain the formation of a disordered system of nanowhiskers, which do not have defined directions and intersect each other at angles of $45°$ and $90°$. The star-like structure indicates that the growth of whiskers occurred from nucleation centers on the substrate surface.

Considering this growth mechanism, further research can be conducted to optimize the growth conditions and control the morphology of the nanowhiskers, which can lead to improved properties and the expansion of possible applications of $Al_xGa_{1-x}As$-based nanostructures.

It is also important to note that according to the established explanations of film growth on semiconductor surfaces, there are three mechanisms:

- The Frank–van der Merwe growth mechanism is characterized by layer-by-layer film growth and is typical for cases where the crystalline lattices of the substrate and film are well matched [63];
- The Volmer–Weber mechanism, on the contrary, is characterized by island growth and occurs mainly in cases where the crystalline lattices have pretty different parameters [64];
- The Stranski–Krastanov mechanism is characterized by layer-plus-island growth and is a "compromise mechanism" [65].

Given that the crystalline lattices of AlAs, GaAs, and $Al_xGa_{1-x}As$ demonstrate remarkable parameter similarity, we should have observed a layer-by-layer film growth mechanism. However, we see the formation of thin nanowhiskers, which then merge into islands. The discrepancy between the theoretical models and experimental data can be explained by understanding that we intentionally pre-etched the GaAs surface, which allowed us to alter the formation mechanism of $Al_xGa_{1-x}As$ on the GaAs surface. According to the authors, structures with a developed morphology, particularly nanowhiskers, may have several advantages over thin films for use in solar cells. For instance, they can provide a larger surface area for light absorption, increasing light energy conversion efficiency.

Using structures with a developed morphology, such as nanowhiskers, can also help reduce energy losses due to surface recombination because these structures typically have high surface quality. Furthermore, these structures can be grown on related substrates using straightforward methods (in our case, electrochemical deposition), which reduces the cost of solar cell production.

The $Al_xGa_{1-x}As$ nanowhisker layer on the GaAs surface offers promising prospects for photocatalytic applications. With a bandgap (Eg) of 2.067 eV, it falls within the suitable range for the efficient absorption of visible light, making it potentially active in a broader spectrum of light for photocatalytic reactions. Its relatively wide bandgap also ensures photostability under irradiation conditions, preventing it from photocorrosion or degradation. The developed morphology, characterized by nanowhiskers, provides an expansive effective surface area, which is pivotal for maximizing the interaction with reactants, thus amplifying the photocatalytic efficiency. This attribute, combined with the intrinsic semiconducting properties of $Al_xGa_{1-x}As$, can lead to higher charge separation efficiencies

and reduced recombination rates. Given the noted advantages and their fabrication using cost-effective electrochemical deposition, $Al_xGa_{1-x}As$ nanowhisker layers exhibit strong potential in photocatalysis, warranting more profound explorative studies in this direction.

Therefore, further research is needed on the growth mechanisms of $Al_xGa_{1-x}As$ nanowhiskers on the GaAs surface, the ability to adjust the "x" parameter during growth using electrochemical methods, and the light-absorbing properties of the formed compounds for their use in solar cells. Moreover, to harness the full potential of $Al_xGa_{1-x}As$ nanowhiskers in photocatalytic applications, further research into doping techniques with transition metals, such as Fe, Ni, and V, is crucial as they can introduce novel properties and enhance the efficiency of the photocatalytic processes.

5. Conclusions

This study demonstrated the feasibility of growing $Al_xGa_{1-x}As$ nanowhiskers on a GaAs surface using a simple, cost-effective electrochemical deposition method. The initial preparation involved structuring the GaAs surface by electrochemical etching. This approach led to the formation of a branched system of nanowhiskers, thereby creating a continuous layer of islands.

An in-depth investigation of the obtained compound's structural, morphological, and compositional attributes was conducted. X-ray diffraction analysis revealed the presence of spectra corresponding to $Al_{0.71}Ga_{0.29}As$, AlAs, and GaAs. Notably, these three compounds exhibit almost identical crystal lattice parameters, adding a layer of complexity to their interpretation.

Further examination of the photoluminescence spectrum indicated a bandgap width of 2.067 eV for $Al_{0.71}Ga_{0.29}As$ (x = 0.71), displaying a slight blue shift from the theoretical value of Eg = 2.016 eV. We attribute this shift to the augmentation of quantum confinement effects that are intimately related to size quantization effects. Our findings underscore the excellent crystallinity and uniformity of the structure.

Interestingly, despite the striking similarity in the crystal lattices of AlAs, GaAs, and $Al_xGa_{1-x}As$, we observed the formation of nanowhiskers rather than a layer-by-layer film growth. We postulate that the discrepancy between the theoretical models and experimental data lies in the effect of the initial etching of GaAs on the formation mechanism of $Al_xGa_{1-x}As$ on the GaAs surface.

The intriguing morphology of these nanowhiskers offers promising applications in solar cells, as they provide a larger surface area for light absorption and reduce energy losses due to surface recombination. Furthermore, they may offer a pathway to improve the cost-effectiveness of solar cell production because of their synthesis through simple, scalable methods, such as electrochemical deposition.

In conclusion, our work offers insights into the electrochemical deposition method as a flexible, cost-effective tool for fabricating a broad class of two- and three-dimensional materials. Future investigations should focus on the growth mechanisms of $Al_xGa_{1-x}As$ nanowhiskers, the feasibility of adjusting the "x" parameter during electrochemical deposition, and a detailed study of the light-absorbing properties of the formed compounds. Our findings lay the groundwork for optimizing the growth conditions and control of nanowhisker morphology, contributing to improving their properties and potential application in solar cells.

Author Contributions: Conceptualization, Y.S. and A.I.P.; Methodology, Y.S. and S.K.; Software, S.K.; Validation, S.K.; Formal analysis, Y.S., S.K., I.K. and A.A.A.; Investigation, Y.S. and I.B.; Resources, Y.S., I.B. and A.I.P.; Writing—original draft, Y.S. and I.B.; Writing—review and editing, I.K., A.A.A. and A.I.P.; Funding acquisition, A.I.P. All authors have read and agreed to the published version of the manuscript.

Data Availability Statement: Data is contained within the article.

Conflicts of Interest: The authors declare no conflict of interest.

References

1. Su, Z.; Yang, Y.; Huang, Q.; Chen, R.; Ge, W.; Fang, Z.; Huang, F.; Wang, X. Designed biomass materials for "green" electronics: A review of materials, fabrications, devices, and perspectives. *Prog. Mater. Sci.* **2022**, *125*, 100917. [CrossRef]
2. Mahmood, K.; Sarwar, S.; Mehran, M.T. Current status of electron transport layers in perovskite solar cells: Materials and properties. *RSC Adv.* **2017**, *7*, 17044–17062. [CrossRef]
3. Suchikova, Y.A.; Kidalov, V.V.; Sukach, G.A. Influence of the carrier concentration of indium phosphide on the porous layer formation. *J. Nano Electron. Phys.* **2010**, *2*, 75–81.
4. Vadakkedath Gopi, S.; Spalatu, N.; Basnayaka, M.; Krautmann, R.; Katerski, A.; Josepson, R.; Grzibovskis, R.; Vembris, A.; Oja Acik, I. Post deposition annealing effect on properties of CdS films and its impact on CdS/Sb$_2$Se$_3$ solar cells performance. *Front. Energy Res.* **2023**, *11*, 1162576. [CrossRef]
5. Liudziute, M.; Zalenkiene, S.; Ivanauskas, R.; Ancutiene, I. Impact of Polyamide Surface Preparation on the Formation of Mixed CdS-CdTe Layers. *Crystals* **2023**, *13*, 730. [CrossRef]
6. Balakhayeva, R.; Akilbekov, A.; Baimukhanov, Z.; Usseinov, A.; Giniyatova, S.; Zdorovets, M.; Vlasukova, L.; Popov, A.I.; Dauletbekova, A. CdTe Nanocrystal Synthesis in SiO$_2$/Si Ion-Track Template: The Study of Electronic and Structural Properties. *Phys. Status Solidi* **2021**, *218*, 2000231. [CrossRef]
7. Heredia-Cancino, J.A.; Mendoza-Peña, K.J.; Higuera-Valenzuela, H.J.; Soto, B.M.A.; Ochoa-Landín, R.; Castillo, S.J. Synthesis Optimization of Cadmium Carbonate Films as Potential Precursor to Produce CdSe, CdTe, and CdO Films. *Coatings* **2022**, *12*, 1691. [CrossRef]
8. Kalyk, F.; Žalga, A.; Vasiliauskas, A.; Tamulevičius, T.; Tamulevičius, S.; Abakevičienė, B. Synthesis and Electron-Beam Evaporation of Gadolinium-Doped Ceria Thin Films. *Coatings* **2022**, *12*, 747. [CrossRef]
9. Tamulevičius, S.; Valkonen, M.P.; Laukaitis, G.; Lindroos, S.; Leskelä, M. Stress and surface studies of SILAR grown CdS thin films on GaAs (100). *Thin Solid Film.* **1999**, *355*, 430–434. [CrossRef]
10. Ščajev, P.; Miasojedovas, S.; Mekys, A.; Onufrijevs, P.; Cheng, H.-H. Time-Resolved Photoluminescence in GeSn Film by New Infrared Streak Camera Attachment Based on a Broadband Light Upconversion. *Coatings* **2023**, *13*, 111. [CrossRef]
11. Levinas, R.; Tsyntsaru, N.; Cesiulis, H.; Viter, R.; Grundsteins, K.; Tamašauskaitė-Tamašiūnaitė, L.; Norkus, E. Electrochemical Synthesis of a WO$_3$/MoS$_x$ Heterostructured Bifunctional Catalyst for Efficient Overall Water Splitting. *Coatings* **2023**, *13*, 673. [CrossRef]
12. Vihodceva, S.; Šutka, A.; Otsus, M.; Vija, H.; Grase, L.; Kahru, A.; Kasemets, K. Visible-Light Active Flexible and Durable Photocatalytic Antibacterial Ethylene-co-vinyl Acetate—Ag/AgCl/α-Fe$_2$O$_3$ Composite Coating. *Nanomaterials* **2022**, *12*, 1984. [CrossRef] [PubMed]
13. Balakhayeva, R.; Akilbekov, A.; Baimukhanov, Z.; Giniyatova, S.; Zdorovets, M.; Gorin, Y.; Popov, A.I.; Dauletbekova, A. Structure properties of CdTe nanocrystals created in SiO$_2$/Si ion track Templates. *Surf. Coat. Technol.* **2020**, *401*, 126269. [CrossRef]
14. Karipbayev, Z.T.; Kumarbekov, K.; Manika, I.; Suchikova, Y.; Popov, A.I. Optical, Structural, and Mechanical Properties of Gd$_3$Ga$_5$O$_{12}$ Single Crystals Irradiated with [84]Kr$^+$ Ions. *Phys. Status Solidi B* **2022**, *259*, 2100415. [CrossRef]
15. Yana, S. Porous indium phosphide: Preparation and properties. In *Handbook of Nanoelectrochemistry: Electrochemical Synthesis Methods, Properties, and Characterization Techniques*, 1st ed.; Springer: Cham, Switzerland, 2016; pp. 283–306. [CrossRef]
16. Suchikova, Y.; Kovachov, S.; Bohdanov, I.; Moskina, A.; Popov, A. Characterization of Cd$_x$Te$_y$O$_z$/CdS/ZnO Heterostructures Synthesized by the SILAR Method. *Coatings* **2023**, *13*, 639. [CrossRef]
17. Suchikova, Y.; Kovachov, S.; Bohdanov, I.; Karipbaev, Z.T.; Pankratov, V.; Popov, A.I. Study of the structural and morphological characteristics of the Cd$_x$Te$_y$O$_z$ nanocomposite obtained on the surface of the CdS/ZnO heterostructure by the SILAR method. *Appl. Phys. A* **2023**, *129*, 499. [CrossRef]

18. Grechenkov, J.; Gopejenko, A.; Bocharov, D.; Isakoviča, I.; Popov, A.I.; Brik, M.G.; Piskunov, S. Ab Initio Modeling of CuGa1−xInxS2, CuGaS$_{2(1-x)}$Se$_{2x}$ and Ag$_{1-x}$Cu$_x$GaS$_2$ Chalcopyrite Solid Solutions for Photovoltaic Applications. *Energies* **2023**, *16*, 4823. [CrossRef]

19. Kılıç, H.S.; Gezgin, S.Y.; Üzüm, Ö.; Gündoğdu, Y. Third order nonlinear optical properties of copper indium gallium selenide (CIGS) nanocrystal thin films. *Appl. Phys. B* **2022**, *128*, 105. [CrossRef]

20. Sychikova, Y.A.; Kidalov, V.V.; Sukach, G.A. Dependence of the threshold voltage in indium-phosphide pore formation on the electrolyte composition. *J. Surface Investig.* **2013**, *7*, 626–630. [CrossRef]

21. Suohikova, Y.; Vambol, S.; Vambol, V.; Mozaffari, N. Justification of the most rational method for the nanostructures synthesis on the semiconductors surface. *J. Achiev. Mater. Manuf. Eng.* **2019**, *92*, 19–28. [CrossRef]

22. Vambol, S.O.; Bogdanov, I.T.; Vambol, V.V.; Suchikova, Y.O.; Kovachov, S.S. Correlation between technological factors of synthesis of por-GaP and its acquired properties. *Nanosist. Nanomater. Nanotehnol.* **2018**, *16*, 657–670.

23. Foell, H.; Langa, S.; Carstensen, J.; Christophersen, M.; Tiginyanu, I.M. Pores in III–V semiconductors. *Adv. Mater.* **2003**, *15*, 183–198. [CrossRef]

24. Langa, S.; Carstensen, J.; Christophersen, M.; Steen, K.; Frey, S.; Tiginyanu, I.M.; Föll, H. Uniform and nonuniform nucleation of pores during the anodization of Si, Ge, and III-V semiconductors. *J. Electrochem. Soc.* **2005**, *152*, C525. [CrossRef]

25. Zhang, L.; Zheng, Z.; Lou, X. A review of WBG and Si devices hybrid applications. *Chin. J. Electr. Eng.* **2021**, *7*, 1–20. [CrossRef]

26. Sobolev, M.S.; Ilkiv, I.V.; Lazarenko, A.A.; Mizerov, A.M.; Nikitina, E.V.; Pirogov, E.V.; Bouravleuv, A.D. Monolith GaAsP/Si dual-junction solar cells grown by MBE. *J. Phys. Conf. Ser.* **2019**, *1410*, 012040. [CrossRef]

27. Zhang, W.W.; Qi, H.; Ji, Y.K.; He, M.J.; Ren, Y.T.; Li, Y. Boosting photoelectric performance of thin film GaAs solar cell based on multi-objective optimization for solar energy utilization. *Solar Energy* **2021**, *230*, 1122–1132. [CrossRef]

28. Ajayan, J.; Nirmal, D.; Mohankumar, P.; Kuriyan, D.; Fletcher, A.A.; Arivazhagan, L.; Kumar, B.S. GaAs metamorphic high electron mobility transistors for future deep space-biomedical-millitary and communication system applications: A review. *Microelectron. J.* **2019**, *92*, 104604. [CrossRef]

29. Steiner, M.A.; France, R.M.; Buencuerpo, J.; Geisz, J.F.; Nielsen, M.P.; Pusch, A.; Olavarria, W.J.; Young, M.; Ekins-Daukes, N.J. High efficiency inverted GaAs and GaInP/GaAs solar cells with strain-balanced GaInAs/GaAsP quantum wells. *Adv. Energy Mater.* **2020**, *11*, 2002874. [CrossRef]

30. Quandt, D.; Arsenijević, D.; Strittmatter, A.; Bimberg, D.H. Static and Dynamic Characteristics of In (AsSb)/GaAs Submonolayer Lasers. *EEE J. Quantum Electron.* **2019**, *55*, 1–7. [CrossRef]

31. Zhang, J.; Itzler, M.A.; Zbinden, H.; Pan, J.W. Advances in InGaAs/InP single-photon detector systems for quantum communication. *Light. Sci. Appl.* **2015**, *4*, e286. [CrossRef]

32. Lindsey, Z.R.; West, M.; Jacobson, P.; Ray, J.R. Benchtop Electrochemical Growth and Controlled Alloying of Polycrystalline In x Ga1–x As Thin Films. *Cryst. Growth Des.* **2022**, *22*, 4228–4235. [CrossRef]

33. Zhang, X.; Yi, R.; Gagrani, N.; Li, Z.; Zhang, F.; Gan, X.; Yao, X.; Yuan, X.; Wang, N.; Zhao, J.; et al. Ultralow Threshold, Single-Mode InGaAs/GaAs Multiquantum Disk Nanowire Lasers. *ACS Nano* **2021**, *15*, 9126–9133. [CrossRef] [PubMed]

34. Woods-Robinson, R.; Han, Y.; Zhang, H.; Ablekim, T.; Khan, I.; Persson, K.A.; Zakutayev, A. Wide band gap chalcogenide semiconductors. *Chem. Rev.* **2020**, *120*, 4007–4055. [CrossRef] [PubMed]

35. Zhang, B.; Wang, S. A survey of EMI research in power electronics systems with wide-bandgap semiconductor devices. *IEEE J. Emerg. Sel. Top. Power Electron.* **2019**, *8*, 626–643. [CrossRef]

36. Shur, M. Wide band gap semiconductor technology: State-of-the-art. *Solid-State Electron.* **2019**, *155*, 65–75. [CrossRef]

37. Zheng, S.; Xiao, S.; Peng, K.; Pan, Y.; Yang, X.; Lu, X.; Han, G.; Zhang, B.; Zhou, Z.; Wang, G.; et al. Symmetry-Guaranteed High Carrier Mobility in Quasi-2D Thermoelectric Semiconductors. *Adv. Mater.* **2023**, *35*, 2210380. [CrossRef]

38. Gil-Corrales, J.A.; Morales, A.L.; Yücel, M.B.; Kasapoglu, E.; Duque, C.A. Electronic Transport Properties in GaAs/AlGaAs and InSe/InP Finite Superlattices under the Effect of a Non-Resonant Intense Laser Field and Considering Geometric Modifications. *Int. J. Mol. Sci.* **2022**, *23*, 5169. [CrossRef] [PubMed]

39. Kawaharazuka, A.; Onomitsu, K.; Nishinaga, J.; Horikoshi, Y. Effect of excitons on the absorption in the solar-cell with Al-GaAs/GaAs superlattice grown by molecular beam epitaxy. *J. Cryst. Growth* **2011**, *323*, 504–507. [CrossRef]

40. Bahar, M.K.; Rodríguez-Magdaleno, K.A.; Martínez-Orozco, J.C.; Mora-Ramos, M.E.; Ungan, F.A.T. Optical properties of a triple AlGaAs/GaAs quantum well purported for quantum cascade laser active region. *Mater. Today Commun.* **2020**, *26*, 101936. [CrossRef]

41. Suchikova, Y.O.; Kovachov, S.S.; Lazarenko, A.S.; Bardus, I.O.; Tikhovod, K.; Hurenko, O.I.; Bohdanov, I.T. Oxidation of the n-GaAs Surface: Morphological and Kinetic Analysis. *J. Nano-Electron. Phys.* **2022**, *14*, 03033. [CrossRef]

42. Suchikova, Y.; Lazarenko, A.; Kovachov, S.; Usseinov, A.; Karipbaev, Z.; Popov, A.I. Formation of porous Ga$_2$O$_3$/GaAs layers for electronic devices. In Proceedings of the 16th International Conference on Advanced Trends in Radioelectronics, Telecommunications and Computer Engineering, TCSET, Lviv-Slavske, Ukraine, 22–26 February 2022; pp. 410–413. [CrossRef]

43. Kovachov, S.; Bohdanov, I.; Karipbayev, Z.; Suchikova, Y.; Tsebriienko, T.; Popov, A.I. Layer-by-Layer Synthesis and Analysis of the Phase Composition of Cd$_x$Te$_y$O$_z$/CdS/por-ZnO/ZnO Heterostructure. In Proceedings of the 2022 IEEE 3rd KhPI Week on Advanced Technology, KhPI Week, Kharkiv, Ukraine, 3–7 October 2022. [CrossRef]

44. Kovachov, S.; Bohdanov, I.; Bardus, I.; Drozhcha, D.; Tikhovod, K.; Khrekin, A.; Bondarenko, V.; Kosogov, I.; Suchikova, Y. About synthesis mechanism of periodic oxide nanocrystallites on surface of single-crystal. *Phys. Chem. Solid State* **2023**, *24*, 159–165. [CrossRef]

45. Suchikova, Y.; Bogdanov, I.; Kovachov, S.; Kamensky, D.; Myroshnychenko, V.; Panova, N. Optimal ranges determination of morphological parameters of nanopatterned semiconductors quality for solar cells. *Arch. Mater. Sci. Eng.* **2020**, *1*, 15–24. [CrossRef]

46. Ko, F.K.; Kuznetsov, V.; Flahaut, E.; Peigney, A.; Laurent, C.; Prinz, V.Y.; Mani, R.C.; Sunkara, M.K.; Baldwin, R.P.; Capelli, E.; et al. Formation of Nanofibers and Nanotubes Production. In *Nanoengineered Nanofibrous Materials*; Guceri, S., Gogotsi, Y.G., Kuznetsov, V., Eds.; NATO Science Series 169; Springer: Dordrecht, The Netherlands, 2004. [CrossRef]

47. Shetti, N.P.; Malode, S.J.; Nayak, D.S.; Bagihalli, G.B.; Kalanur, S.S.; Malladi, R.S.; Reddy, C.V.; Aminabhavi, T.M.; Reddy, K.R. Fabrication of ZnO nanoparticles modified sensor for electrochemical oxidation of methdilazine. *Appl. Surf. Sci.* **2019**, *496*, 143656. [CrossRef]

48. Bisquert, J.; Fabregat-Santiago, F.; Mora-Seró, I.; Garcia-Belmonte, G.; Barea, E.M.; Palomares, E. A review of recent results on electrochemical determination of the density of electronic states of nanostructured metal-oxide semiconductors and organic hole conductors. *Inorg. Chim. Acta* **2008**, *361*, 684–698. [CrossRef]

49. Islam, S.; Mia, M.; Shah, S.S.; Naher, S.; Shaikh, M.N.; Aziz, A.; Ahammad, A.J.S. Recent Advancements in Electrochemical Deposition of Metal-Based Electrode Materials for Electrochemical Supercapacitors. *Chem. Rec.* **2022**, *22*, e202200013. [CrossRef] [PubMed]

50. Liu, X.; Wang, F.; Wang, Q. Nanostructure-based WO_3 photoanodes for photoelectrochemical water splitting. *Phys. Chem. Chem. Phys.* **2012**, *14*, 7894–7911. [CrossRef]

51. Suchikova, Y.; Kovachov, S.; Bohdanov, I. Formation of oxide crystallites on the porous GaAs surface by electrochemical deposition. *Nanomater. Nanotechnol.* **2022**, *12*, 1–12. [CrossRef]

52. Vambol, S.O.; Bohdanov, I.T.; Vambol, V.V.; Nestorenko, T.P.; Onyschenko, S.V. Formation of filamentary structures of oxide on the surface of monocrystalline gallium arsenide. *J. Nano-Electron. Phys.* **2017**, *9*, 06016. [CrossRef]

53. Scherrer, P. Determination of the size and internal structure of colloidal particles using X-rays. *Nachr. Ges. Wiss. Göttingen* **1918**, *2*, 98–100.

54. Langford, J.; Wilson, A. Scherrer after sixty years: A survey and some new results in the determination of crystallite size. *J. Appl. Crystallogr.* **1978**, *11*, 102–113. [CrossRef]

55. Kuryliuk, V.; Podolian, A.; Korotchenkov, O. Acoustically driven charge separation in semiconductor heterostructures sensed by optical spectroscopy techniques. *Open Phys.* **2010**, *8*, 1. [CrossRef]

56. Kim, O.K.; Spitzer, W.G. Infrared reflectivity spectra and Raman spectra of Ga1−xAlxAs mixed crystals. *J. Appl. Phys.* **1979**, *50*, 4362–4370. [CrossRef]

57. Nakahara, J.; Ichimori, T.; Minomura, S.; Kukimoto, H. Raman Spectra in AlxGa1-xAs under High Pressure. *J. Phys. Soc. Jpn.* **1987**, *56*, 1010–1016. [CrossRef]

58. Guo, L.W.; Han, Y.J.; Hu, C.Y.; Tan, P.H.; Yang, F.H.; Huang, Q.; Zhou, J.M. Raman study of low-temperature-grown $Al_{0.29}Ga_{0.71}As$/GaAs photorefractive materials. *Phys. Rev. B* **2002**, *65*, 125325. [CrossRef]

59. Wang, Y.; Zahid, F.; Zhu, Y.; Wang, J.; Guo, H. Band offset of GaAs/$Al_xGa_{1−x}$As heterojunctions from atomistic first principles. *Appl. Phys. Lett.* **2013**, *102*, 132109. [CrossRef]

60. Adachi, S. *GaAs and Related Materials*; World Scientific: Singapore, 1994. [CrossRef]

61. Brown, M.A.; Abbas, Z.; Kleibert, A.; May, S.; Squires, T.M. Determination of surface potential and electrical double-layer structure at the aqueous electrolyte-nanoparticle interface. *Phys. Rev. X* **2016**, *6*, 011007. [CrossRef]

62. Suchikova, Y.; Kovachov, S.; Lazarenko, A.; Bohdanov, I. Research of synthesis conditions and structural features of heterostructure $Al_XGa_{1−X}$As/GaAs of the 'desert rose' type. *Appl. Surf. Sci. Adv.* **2022**, *12*, 100327. [CrossRef]

63. Sun, X.W.; Huang, H.C.; Kwok, H.S. On the initial growth of indium tin oxide on glass. *Appl. Phys. Lett.* **1996**, *68*, 2663–2665. [CrossRef]

64. Floro, J.A.; Hearne, S.J.; Hunter, J.A.; Seel, S.C.; Thompson, C.V. The dynamic competition between stress generation and relaxation mechanisms during coalescence of Volmer-Weber thin films. *J. Appl. Phys.* **2001**, *89*, 4886–4897. [CrossRef]

65. Pan, L.; Lew, K.-K.; Redwing, J.M.; Dickey, E.C. Stranski-Krastanow growth of germanium on silicon nanowires. *Nano Lett.* **2005**, *5*, 1081–1085. [CrossRef]